DOI: 10.13009/EUCASS2019-492

DOI: ADD DOI NUMBER HERE

Optimisation in Active Flow Separation Control in Low-Pressure Turbines

Yinzhu Wang[⋆]*, Jorge Saavedra*[•]*, Esteban Ferrer*[⋆†]*, Guillermo Paniagua*[•] *and Eusebio Valero*[⋆]
[⋆]*ETSIAE-UPM - Escuela Técnica Superior de Ingeniería Aeronáutica y del Espacio - Universidad Politécnica de Madrid*
Plaza de Cardenal Cisneros 3, 28040, Madrid, Spain
[•]*Mechanical Engineering, Purdue University*
West Lafayette, 47907, IN, USA
y.wang@upm.es
[†]Corresponding author

Abstract

Boundary layer separation significantly affects the aerothermal performance of low-pressure turbines in flight vehicles at high altitude. In this investigation, we present the aft portion of the suction side of a low-pressure turbine as a wall mounted hump, where the flow diffusion could lead to boundary layer detachment at low Reynolds numbers and fully attached flow is present at higher Reynolds numbers. The goal of the current research is to find an effective flow control approach to prevent the boundary layer detachment and reduce dynamic head pressure loss with a minimum energy requirements.

Stability and sensitivity analysis on the flow is conducted. Assisted with all the information from stability and structural sensitivity analysis, we perform an optimisation investigation to find the optimal location and blow rate of the injection. The optimal location and blow rate inhibit the separated flow regions exposed to transient mean flow conditions.

In this investigation, we prove the feasibility of finding an optimal flow control strategy that considers the inherent transient behaviour of the flow by optimisation.

Contents

DOI: 10.13009/EUCASS2019-492

1. Introduction

Unmanned flight vehicles for operations at a large envelope of altitude have met an uprising demand in recent years. One specific challenge in the designing flight vehicle is the development of an engine that adapts a large range of Reynolds numbers.

The operating Reynolds number during high-altitude cruise for the low-pressure turbines (LPT) in a flight vehicle can drop drastically compared to the operating conditions at low altitude. However, the development of more compact and versatile distributed-thrust engine has been constrained by the occurrence of flow separation in low-pressure turbine airfoils.[2,9,22,27] At low Reynolds numbers (below the order of 10^6, based on the airfoil chord and inlet velocity), the rear part of the suction side of the airfoil can experience flow separation which increases the pressure loss and reduces the efficiency of the turbine blades, which, therefore affects the performance of the flight vehicle at high altitude.

Passive flow control techniques are mainly aimed at the use of geometrical elements to promote laminar to turbulent boundary layer transition. Passive control techniques require no energy input or complicated actuation mechanisms, which makes it easier to implement. Lake et al.[16] introduced the use of surface dimples to reduce the size of the separated flow regions. Volino[30] investigated on the effect of rectangular bars on the suction side surface to promote the boundary layer transition and encourage the flow reattachment. However, the added geometrical elements or a deformation based on the original configuration, alter the performance greatly at off-design conditions.

Comparing to passive control techniques, active flow control techniques are able to adjust the parameters in the control strategies to adapt to different operating conditions. Greenblatt and Wygnanski[11] documented the control of flow separation by periodic excitation with a hydrodynamic approach, ranging from acoustic wave-based approaches to flow injection and ingestion. The application of glow discharge plasma actuation on the boundary layer control has been experimentally[13] and numerically[24] proven to enhance a fast flow reattachment.

Flow stability analysis[28] predicts how small flow perturbations grow or decay with respect to an equilibrium flow solution (the base flow), providing information about the onset of the physical mechanisms (reported as modes) responsible for detachments can help to determine means by which to control it.

The linear stability community has developed tools to control the onset of unfavoured modes, which have been popularised as adjoint-based sensitivity analysis. Sensitivity analysis identifies the regions of the flow that, if modified, lead to the greatest damping (or amplification) of the feature responsible for the instability. The numerical study of flow sensitivity relies on the use of adjoints.[17] The importance of adjoints and sensitivity maps, together with the mathematical tools required for the study of the sensitive flow regions, to different parameters, were first introduced by Hill,[12] and have been used extensively to examine the receptivity to internal and external modifications,[8,17,20] and also by the authors.[3,5,6,10,15] Having determined the most sensitive flow regions, it becomes relatively simple to apply a flow control technique. Passive control introduces inactive objects (e.g. a small cylinder), which modifies the flow to stabilise or modify the frequency of particular flow features.[20] Useful active flow control may also be derived from sensitivity maps to control undesirable instabilities.[29]

In recent years, aerodynamic shape optimisation has become a valuable tool for the design of efficient lifting surfaces and even entire aircraft.[23] The advances in computing power and development of more accurate computational fluid dynamics solvers have promoted optimal shape design.[14] In most recent research, aerodynamic optimisation has been successfully applied to optimal flow control strategies.[7,26,31]

In this work, we investigate on the detachment recirculation at the wall mounted hump and the difference of the recirculation bubble sizes at different Reynolds numbers. We identify the modes and structures that dominate the unsteady flow behaviour of the recirculated flow region with stability analysis. In the optimisation investigation, we find an optimal injection strategy within the designated range of parameters.

2. Methodology

2.1 Navier-Stocks Equations

In the present study, we use DLR-TAU code for the simulations. The DLR-TAU code is a compressible three-dimensional Navier-Stocks solver. Spatial discretisation uses a finite volume approach. In this formulation, the mass matrix $\mathcal{M} = \int_\Omega dV$ simplifies to the computational cell volumes Ω. When the compressible Navier-Stokes equations are selected, the right hand side $\mathcal{F}(\boldsymbol{q})$ in (10) denotes the divergence of the viscous and convective fluxes:

$$\begin{aligned} \mathcal{F}(\boldsymbol{q}) &= \int_\Omega \nabla \cdot (\boldsymbol{F}_v - \boldsymbol{F}_e) \\ &= \int_{\partial\Omega} (\boldsymbol{F}_v - \boldsymbol{F}_e) \cdot \mathbf{n}, \end{aligned} \tag{1}$$

DOI: 10.13009/EUCASS2019-492

where $\boldsymbol{F}_e$ are the inviscid, or Euler fluxes, and we have used using Gauss' divergence theorem to replace the divergence of the fluxes by the fluxes through the element faces $\partial\Omega$. Convective fluxes are discretised using a second order Van Leer Upwind scheme.

$$\boldsymbol{F}_e = \begin{bmatrix} \rho u & \rho v & \rho w \\ \rho u^2 + p & \rho uv & \rho uw \\ \rho uv & \rho v^2 + p & \rho vw \\ \rho uw & \rho vw & \rho w^2 + p \\ \rho uH & \rho vH & \rho wH \end{bmatrix}, \tag{2}$$

where ρ and H are the density and total enthalpy. Additionally, $\boldsymbol{F}_v$ defines the viscous fluxes:

$$\vec{\boldsymbol{F}}_v = \begin{bmatrix} 0 & 0 & 0 \\ \tau_{xx} & \tau_{xy} & \tau_{xz} \\ \tau_{yx} & \tau_{yy} & \tau_{yz} \\ \tau_{zx} & \tau_{zy} & \tau_{zz} \\ \sum_{j=1}^{3} v_j\tau_{1j} + \kappa T_x & \sum_{j=1}^{3} v_j\tau_{2j} + \kappa T_y & \sum_{j=1}^{3} v_j\tau_{3j} + \kappa T_z \end{bmatrix}, \tag{3}$$

where κ is the thermal conductivity, T_x, T_y and T_z denote the gradients of temperature and the stress tensor $\boldsymbol{\tau}$ is defined as $\boldsymbol{\tau} = \mu(\nabla\vec{v} + (\nabla\vec{v})^T) - 2/3\mu\boldsymbol{I}\nabla\cdot\vec{v}$, with μ the dynamic viscosity, $\vec{v} = (u, v, w)^T$ and $\boldsymbol{I}$ is the three-dimensional identity matrix. In all cases, the Mach number is kept low such that compressible effects are minimum.

2.2 Transition Transport Model

In this work, we adopt a transition transport model, $\gamma - Re_{\theta t}$ model, for the investigation. The model holds two transport equations, one for the intermittency γ and the other for the Reynolds number based on momentum thickness at the transition point, $Re_{\theta t}$. The intermittency γ represents the fraction of time the flow is turbulent at a fixed position in the flow field. It is zero in case of laminar flow and one in case of turbulent flow. In the transition region, γ varies in between zero and one. The transport equation for $Re_{\theta t}$ is controlled by an empirical transition criterion, which is only valid outside of the boundary layer. Inside the boundary layer, the information about transition onset is transported by convection and diffusion terms.

$$\frac{\partial(\rho\gamma)}{\partial t} + \nabla\cdot(\rho\boldsymbol{u}\gamma) - \nabla\cdot((\mu + \frac{\mu_t}{\sigma_\gamma})\nabla\gamma) = \mathcal{P}_\gamma - \mathcal{E}_\gamma, \tag{4}$$

$$\frac{\partial(\rho Re_{\theta t})}{\partial t} + \nabla\cdot(\rho\boldsymbol{u}Re_{\theta t}) - \nabla\cdot(\sigma_{\theta t}(\mu + \mu_t)\nabla Re_{\theta t}) = \mathcal{P}_\theta t. \tag{5}$$

The production term of the intermittency equation is given by

$$\mathcal{P}_\gamma = F_{length}c_{a1}\rho\tilde{S}\sqrt{\gamma F_{onset}}(1 - c_{e1}\gamma), \tag{6}$$

where $\tilde{S}$ is the magnitude of the stain rate and F_{length} is an empirical function that controls the length of the transition area. It is defined by the second transport quantity $Re_{\theta t}$. F_{onset} is used to trigger the intermittency production. The production term of the second transport equation for $Re_{\theta t}$ is given by

$$\mathcal{P}_{\theta t} = c_{\theta t}\frac{\rho}{t}(Re^{\star}_{\theta t} - Re_{\theta t})(1.0 - F_{\theta t}), \tag{7}$$

where $Re^{\star}_{\theta t}$ is obtained from an empirical transition criterion and $F_{\theta t}$ is an empirical function. The destruction or relaminarisation term of the intermittency equation is

$$\mathcal{E}_\gamma = c_{a2}\rho\tilde{\Omega}\gamma F_{turb}(c_{e2}\gamma - 1), \tag{8}$$

where $\tilde{\Omega}$ is the vorticity magnitude and F_{turb} is an empirical function that depends on the viscosity ratio. The constraints for the intermittency equation are

$$c_{e1} = 1.0, \quad c_{a1} = 0.5, \quad c_{e2} = 50.0, \quad c_{a2} = 0.03, \quad \sigma_\gamma = 1.0. \tag{9}$$

DOI: 10.13009/EUCASS2019-492

2.3 Linear Stability Theory

We consider a discrete approach to derive sensitivity fields.[3,21] The discrete method starts by discretising the governing equations to subsequently derive the linearised system; as opposed to first linearising to then discretise (i.e. continuous approach). An advantage of the discrete version is that, being purely algebraic, it does not require the derivation of adjoint equations or adjoint boundary conditions since these are automatically included in the matrix system.

The methodology may be implemented in compressible or incompressible flow solvers. Here we select, without loss of generality, a compressible version of the Navier-Stokes equations, where conservative variables are utilised: $\mathbf{q} = (\rho, \rho u, \rho v; \rho w; \rho e)^T$, where ρ denotes the density, u, v and w are the velocity components and e denotes energy. We start by considering a spatially discretised time varying and non-dimensional system

$$\mathcal{M}\frac{\partial \boldsymbol{q}}{\partial t} = \mathcal{F}(\boldsymbol{q}), \tag{10}$$

where $\mathcal{F}(\boldsymbol{q})$ is a discrete non-linear operator, $\mathcal{M}$ is the mass matrix resulting from the spatial discretisation.

To perform linear instability analysis the state variable $\boldsymbol{q}$ is decomposed into its steady state contribution, $\bar{\boldsymbol{q}}$, and a small perturbation, $\boldsymbol{q'}$ such that $\boldsymbol{q} = \bar{\boldsymbol{q}} + \boldsymbol{q'}$. We proceed by inserting this decomposition into Eq. (10) and linearise the non-linear discrete system using Taylor series (around $\bar{\boldsymbol{q}}$). Subtracting the base flow equation and neglecting second order terms $O(\boldsymbol{q'}^2)$, we obtain a linearised and time varying system for the perturbation field

$$\mathcal{M}\frac{\partial \boldsymbol{q'}}{\partial t} = \mathcal{J}(\bar{\boldsymbol{q}})\boldsymbol{q'} \tag{11}$$

with $\mathcal{J}(\bar{\boldsymbol{q}}) = \left.\frac{\partial \mathcal{F}(\boldsymbol{q})}{\partial \boldsymbol{q}}\right|_{\bar{\boldsymbol{q}}}$ denoting the Jacobian matrix. Eq. (11) may be advanced in time to simulate the growth or decay of perturbation upon the base flow $\bar{\boldsymbol{q}}$.[1,6] Alternatively, it is possible to solve the above perturbation equation in the frequency domain by introducing the ansatz, $\boldsymbol{q'} = \hat{\boldsymbol{q}}e^{\sigma t}$, which leads to a generalised eigenvalue problem

$$\mathcal{J}(\bar{\boldsymbol{q}})\hat{\boldsymbol{q}} = \sigma\mathcal{M}\hat{\boldsymbol{q}}. \tag{12}$$

The eigenvector $\hat{\boldsymbol{q}}$ is the direct mode associated to the complex eigenvalue, $\sigma = \sigma_R + i\sigma_I$, whose real and imaginary components represent the perturbation growth rate and angular frequency.

2.4 Sensitivity Analysis

The localised regions of sensitivity denote the spatial separation between direct and adjoint modes, which is related to the non-normality[4] of the Navier-Stokes equations. The regions where the direct and adjoint modes overlap define the structural sensitivity to localised feedback or wavemaker regions,[8] and relates to the origin of absolute instabilities. These sensitivity maps provide information on the flow regions where a generic force-velocity coupling causes the largest drift in the eigenvalues and hence provides useful information on control strategies to attenuate these instabilities.[3,8,17] Other flow sensitivities, e.g. to base flow modification or steady forcing,[3,5,19,21,25] have been defined in the literature but are not considered here. Generally speaking, sensitivity analyses define the “sweet spots" for the location of passive control mechanisms and the regions where small modifications lead to the largest modification of the eigenmode behaviour (e.g. enhancing its stability).

The structural sensitivity maps can be calculated by solving the eigenvalue problem with the adjoint of the Jacobian matrix of the system.

$$\sigma_{adj}\mathcal{M}\hat{\boldsymbol{q}}_{adj} = \mathcal{J}_{adj}(\bar{\boldsymbol{q}})\hat{\boldsymbol{q}}_{adj}, \tag{13}$$

in which,

$$\mathcal{J}_{adj} = \mathcal{M}^{-1}\mathcal{J}^H\mathcal{M}. \tag{14}$$

When considering the Navier-Stokes equations without non-linear terms, the resulting system, characterised by its Jacobian matrix is symmetric and consequently self-adjoint. In these cases the direct and adjoint modes are identical. When non-linearities are included in the problem, the Jacobian matrix is not self-adjoint, which makes them different. Then it is possible to find the spatial regions where direct and adjoint modes overlap to obtain the wavemaker region, following equation 15.

$$\mathcal{S} = \|\hat{\mathbf{q}}^+\| \cdot \|\hat{\mathbf{q}}\|. \tag{15}$$

DOI: 10.13009/EUCASS2019-492

3. Numerical Results

In this section, we discuss the results from the flow simulations, stability and sensitivity analysis and optimisation. Regarding boundary conditions, a steady actuation with total pressure and total density is imposed at the inlet and the injection inlet. The lower wall with the mount hump is set to be a transition wall. A static pressure is imposed on the exit. Since DLR-TAU is a three-dimensional solver, it only deals with three-dimensional mesh. The two spanwise boundaries are set to be symmetry plane for two-dimensional simulation. All the other wall, including the upper wall of the channel and the walls in the injection chamber, are slip walls.

Boundary name	Boundary Condition	Notes
Inlet	actuation	P_0, ρ_0
Exit	exit-pressure outflow	P
Lower wall	transition	
Upper wall	slip wall	
Symmetry plane	symmetry plane	
Injection inlet	reservoir-pressure inflow	P_0, ρ_0
Injection walls	slip wall	

Table 1: Boundary conditions.

3.1 Flow Simulation

The numerical domain used to model wall mounted hump is displayed in figure 1. Where the outlet of the domain is located five axial cords downstream of the test article. The inlet boundary of the domain is treated a total pressure boundary condition where total pressure and temperature are prescribed together with the turbulent intensity and turbulent length scale. While the outlet is modeled as a back pressure boundary where the static pressure level of the simulation is imposed. The top surface is treated as an adiabatic slip line, while the bottom surface is a viscous isothermal wall. The actual total and static quantities imposed in the numerical evaluations are summarized in table 2.

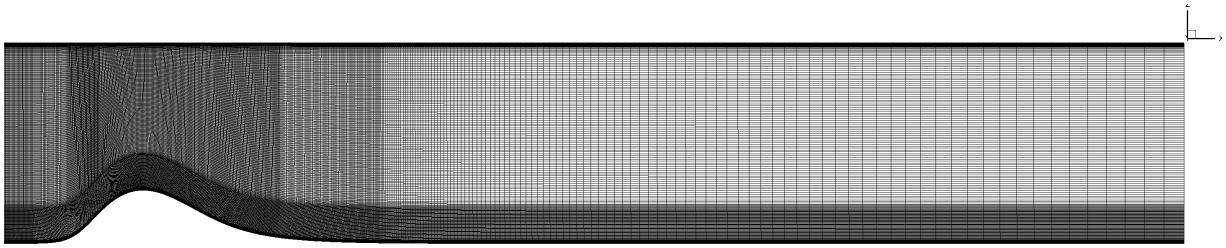

Figure 1: Mesh.

No.	Inlet P_0 $(Pascal)$	Inlet T_0 (K)	Exit P $(Pascal)$	Inlet ρ_0 (kg/m^3)	Re
1	100010	500	100000	0.6969	13980
2	100050	500	100000	0.6972	31261
3	100100	500	100000	0.6976	44214
4	100500	500	100000	0.7003	98928
5	101000	500	100000	0.7038	140016
6	101649	500	100000	0.7084	180000
7	105000	500	100000	0.7317	315013
8	110000	500	100000	0.7666	448759

Table 2: Case list.

The performance of the test article was evaluated at a wide range of Reynolds numbers (based on the chord length and the mean velocity at the inlet) ranging from 13980 up to 448759. The detachment and reattachment locations for each one of the Reynolds explored are shown figure 2.

DOI: 10.13009/EUCASS2019-492

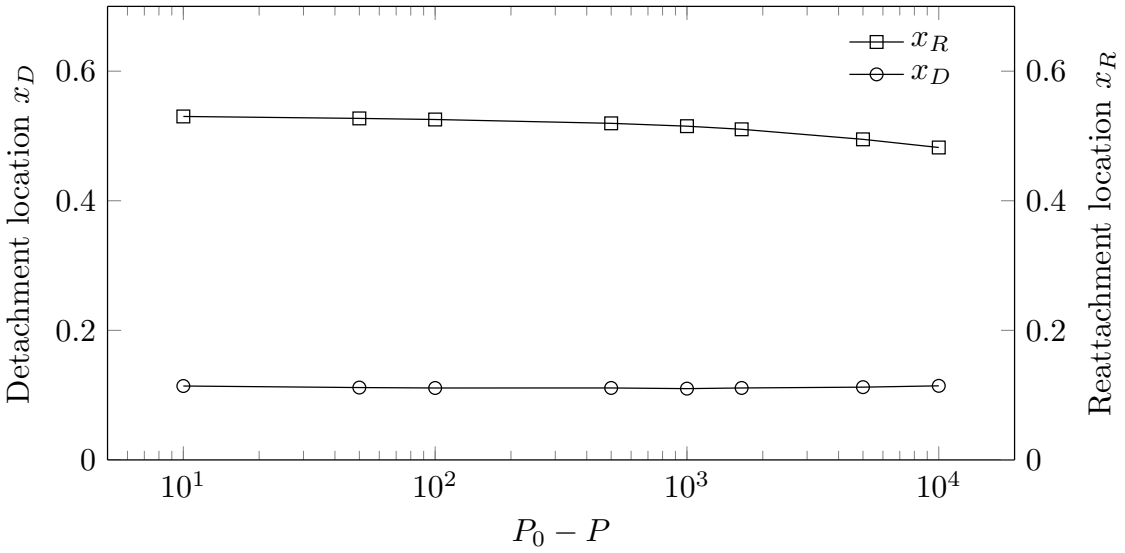

Figure 2: Detachment and reattachment locations against inlet total pressure

As previously identified for this geometry, the boundary layer detachment inception is insensitive to the Reynolds number and the recirculated flow region starts always in the same location. On the contrary, the reattachment location is determined by the actual Reynolds number. As the inlet Reynolds number decreases the near wall region has less flow momentum to overcome the adverse pressure gradient and its capability to reattach weakens. Consequently, the reattachment location moves upstream as the Reynolds number increases. The correspondent axial velocity contours for each one of the inlet total pressures are shown in figure 3. Where the reduction of the recirculated flow region with Reynolds number can also be identified.

3.2 Stability and Sensitivity Analysis

In an attempt to identify the modes and structures that dominate the unsteady flow behaviour of the recirculated flow region an stability analysis is performed. Our goal is to detect the structures that dictate the formation and growth of the detached flow bubble. Once identified, we could introduce flow actuation to alter the performance of separated flow region in an effective manner. Specifically, we carry out stability analyses with inlet total pressure P_0 = 100500 without injection, correspondent to a Reynolds number of 98928. The eigenvalue spectrum is shown in figure 4. An unstable mode is identified at σ (4.272, 0). This mode seems to dominate the growth of the separated flow region and lift off of the momentum boundary layer from the surface. The mode structure is shown in figures 5. Figures 5 a and b represent the axial and normal velocity components representative for the most unstable mode. While figures 5 c and d represent the density and structural sensitivity map respectively. The axial and normal velocity and density identify the maximum strength of the mode right at the boundary layer detachment inception. While the sensitivity contour depicts region of influence of the boundary layer detachment mechanism. These results suggest that for an effective mitigation of the boundary layer detachment the actuation should be located at the origin displayed in the axial velocity contours.

The rest of the modes in the domain do not depict and unstable growth, however the mode at $\sigma = (-0.5436, 2.366)$ results of interest due to its proximity to the unstable threshold. The velocity, density and sensitivity map correspondent to this mode are displayed in figure 6. The origin of this mode is also located slightly downstream of the hump summit, close to the separation inception and its region of influence extends across the recirculated flow region. Hence any alteration of this mode could eventually affect the growth of the recirculated flow region.

The stability analysis seem to conclude that an effective actuation to prevent the detachment of the boundary layer or reduce the extension of the flow region must right downstream of the hump summit. In this work, we propose to control the detachment by injecting further flow momentum to energize the near wall region and overcome the adverse pressure gradient.

DOI: 10.13009/EUCASS2019-492

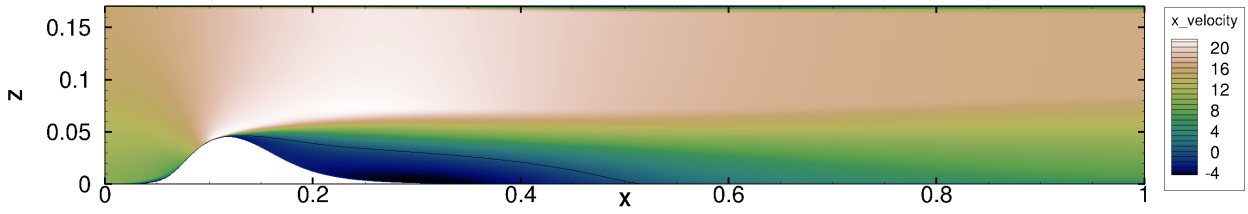

(a) P_0 = 100100.

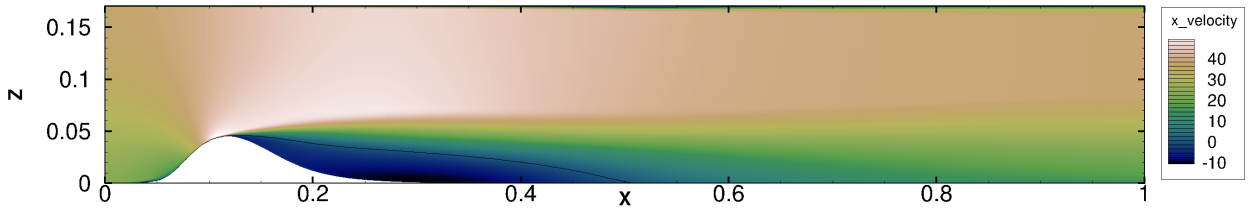

(b) P_0 = 100500.

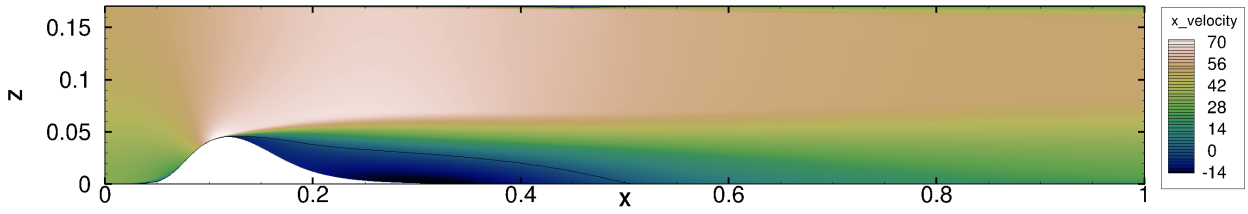

(c) P_0 = 101000.

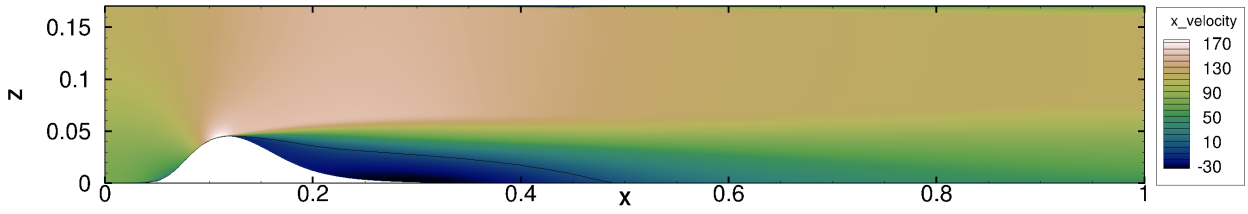

(d) P_0 = 105000.

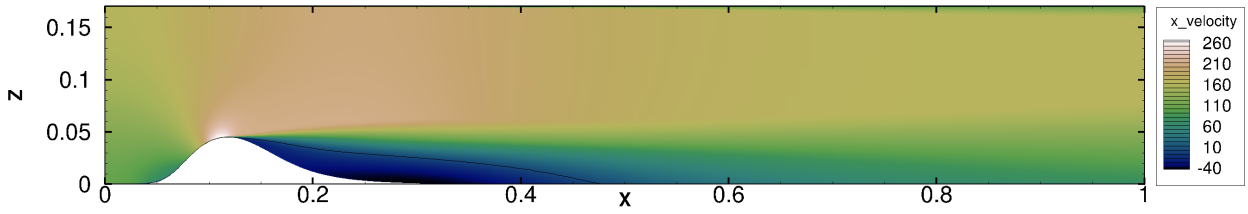

(e) P_0 = 110000.

Figure 3: u_x with different inlet total pressure.

4. Optimisation

4.1 Algorithms and Optimisation Model

In this investigation, we seek to find an optimal location and blow rate to eliminate the recirculation bubble and to maximize the total pressure recovery. the optimization problem is modelled as:

$$\begin{aligned} min: \quad & Pl(\boldsymbol{x_b}, \boldsymbol{R_b}), \\ subject \quad to: \quad & \mathcal{M}\frac{\partial \boldsymbol{q}}{\partial t} = \mathcal{F}(\boldsymbol{q}), \end{aligned} \tag{16}$$

DOI: 10.13009/EUCASS2019-492

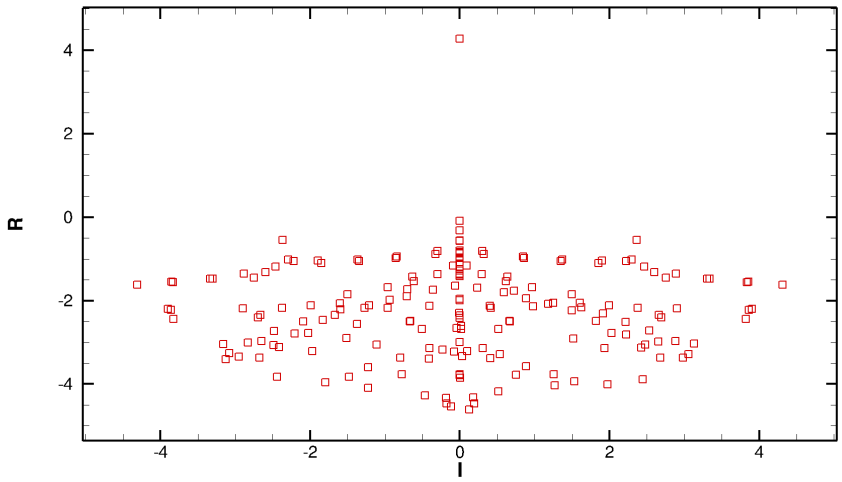

Figure 4: Eigenvalue spectrum, $P_0 = 100500$.

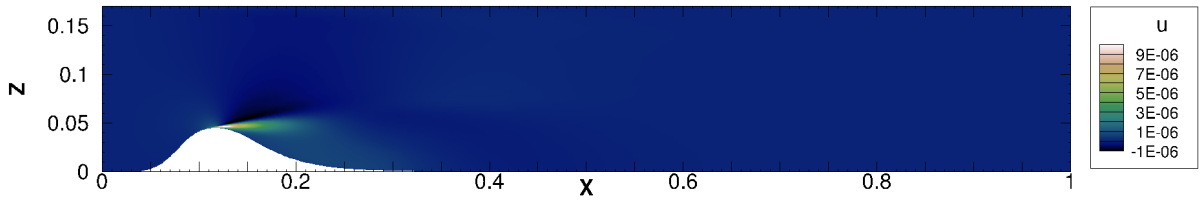

(a) Eigenmode, u_x.

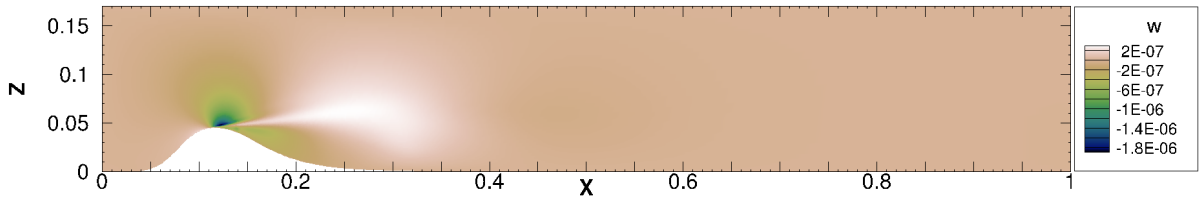

(b) Eigenmode, u_y.

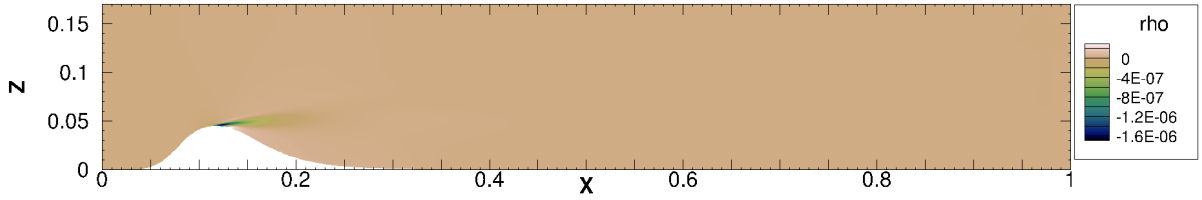

(c) Eigenmode, ρ.

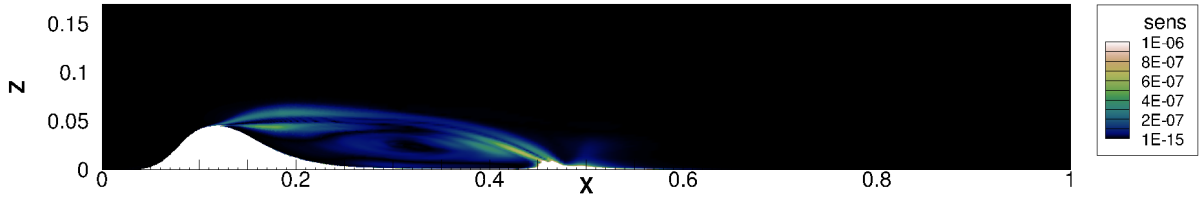

(d) Structural sensitivity map.

Figure 5: Eigenmode and its sensitivity map corresponds to $\sigma = (4.272, 0)$.

DOI: 10.13009/EUCASS2019-492

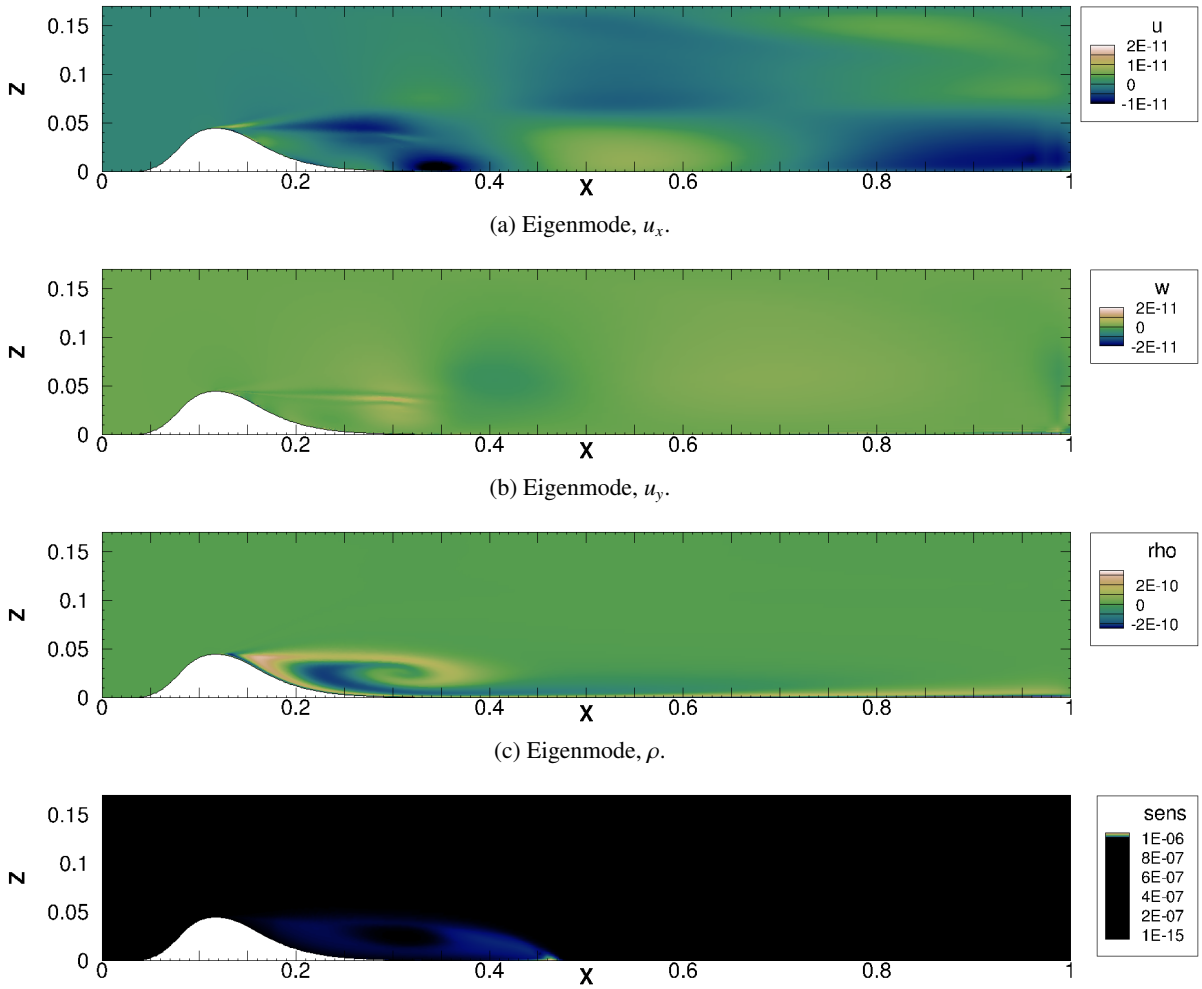

(a) Eigenmode, u_x.

(b) Eigenmode, u_y.

(c) Eigenmode, ρ.

(d) Structural sensitivity map.

Figure 6: Eigenmode and its sensitivity map corresponds to $\sigma = (-0.5436, 2.366)$.

in which, Pl is the dynamic pressure loss, x_b is the xaxial location of the injection, $R_b = (\frac{P_{0,injection}}{P_{0,inlet}} - 1) \times 100\%$ is the blow rate of the injection, in which, $P_{0,injection}$ is the total pressure at the injection inlet, and P_0 is the total pressure at the inlet of the channel. The dynamic pressure loss, Pl, is defined by

$$Pl = \frac{\frac{\int_{\Omega_{Exit}} \frac{1}{2}\rho \boldsymbol{u}^2 P_0 - \int_{\Omega_{Injection}} \frac{1}{2}\rho \boldsymbol{u}^2 P_0}{\int_{\Omega_{Exit}} \frac{1}{2}\rho \boldsymbol{u}^2 + \int_{\Omega_{Injection}} \frac{1}{2}\rho \boldsymbol{u}^2} - \frac{\int_{\Omega_{Inlet}} \frac{1}{2}\rho \boldsymbol{u}^2 P_0}{\int_{\Omega_{Inlet}} \frac{1}{2}\rho \boldsymbol{u}^2}}{\frac{\int_{\Omega_{Inlet}} \frac{1}{2}\rho \boldsymbol{u}^2}{\int_{\Omega_{Inlet}}}}. \tag{17}$$

where the massflow average total pressure is compared to the inlet massflow average total pressure. In addition, to focus the figure of merit on the aerodynamic viscous loses the injected fluid is subtracted from the outlet massflow average quantity.

In this investigation, we adopt a genetic algorithm for the optimisation. The algorithm starts with an initial population (a set of potential solutions), which consists of a number of individuals with combinations of different genes. A gene is a member in a parameter array of an individual. By calling a cost function, the fitness of each individual is evaluated, and the best individuals are selected. After crossover and mutation of genes, new generations with higher fitness are obtained. After a certain amount of iterations, an optimal solution is reached. The procedure of a typical genetic algorithm is shown in Fig. 7. Prior to the optimization, the number of maximum generations, the number of populations, the number of genes, the possibility of crossover and the possibility of mutations, must be specified. The number of genes determines the degrees of freedom to alter each one of the geometries under analysis. While the crossover and mutation possibility identify the variability between successive individuals. The parameters

DOI: 10.13009/EUCASS2019-492

Table 3: Parameters selected for the Genetic Algorithm.

Name	Representation	Value
N_G	Number of maximum generations	500
N_{pop}	Number of population	100
N_g	Number of genes	2
P_x	Possibility of crossover	0.6
P_m	Possibility of mutation	0.6

Table 4: Design of experiment.

Parameter	Number of levels	Minimum	Maximum
x_b	7	0.138	0.175
R_b	9	0	5

retained for our optimisation are summarised in Table 3.

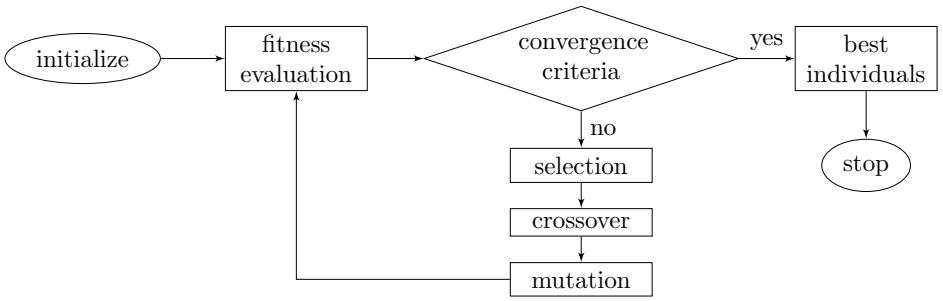

Figure 7: Flow chart of a simple genetic algorithm.

4.2 Surrogate Modelling

To reduce the cost of the overall optimization the use of a surrogate model is adopted. The surrogate model reduces the cost of evaluating the cost function, reducing the impact of uncertainty in evaluation and for easier parallel off-line evaluation. RBF (Radial Basis Function) interpolation is a popular method for constructing surrogates suitable for highly non-linear data using irregular distributions of sample points, which can be adapted to the function being modelled. RBFs have seen increasing use for aerospace applications requiring an interpolation or approximation method, including mesh motion, fluid-structure interaction, and domain element parametrisation, in addition to aircraft data interpolation, owing to the meshless and general nature of the formulation, and tolerable properties of the interpolation kernel.[18]

A Radial Basis Function (RBF) method is a linear combination of a series of basis functions, whose argument is the Euclidean distance between the interpolation point $\boldsymbol{p} = (p_1, p_2, p_3)$ and all the other points in the known data set. The model has the form:

$$Pl(\boldsymbol{p}) = \sum_{i=1}^{N} w_i \phi \|\boldsymbol{p} - \boldsymbol{p}_i\|, \tag{18}$$

where $\boldsymbol{p}$ is the interpolation point, ϕ is the chosen basis function, w_i is the weight coefficient for each basis function, and $\| \bullet \|$ represents the Euclidean norm. Any function ϕ that satisfies the property $\phi(\boldsymbol{p}) = \phi(\|\boldsymbol{p}\|)$ is a radial function, and can be used as a basis function in RBFs. In this work, we select as many RBFs as the number of sampling points for the construction of the surrogate model (see next sections). As applied to the current investigation, $\sigma_R(\boldsymbol{p})$ is the growth rate (real part of the eigenvalue) governed by the geometry parameter array $\boldsymbol{p} = (x_b, R_b)$.

The surrogate model is assisted with a uniform full factorial design of experiment for higher precision. We select 7 and 9 levels for optimisation parameters x_b and R_b, respectively. The details of the design of experiment is shown in table 4.

DOI: 10.13009/EUCASS2019-492

4.3 Optimisation Results

In order to explore the impact of the flow injection along the downstream section of the hump we introduced a cavity inside of the geometry with an outlet along the hump downstream surface. The numerical domain is depicted in figure 8. The main flow boundary conditions remain unaltered and a small cavity with an outlet parallel to the ground level is introduced along the hump. The massflow injection through the slot is controlled by prescribing the total pressure at the bottom surface of the injection cavity.

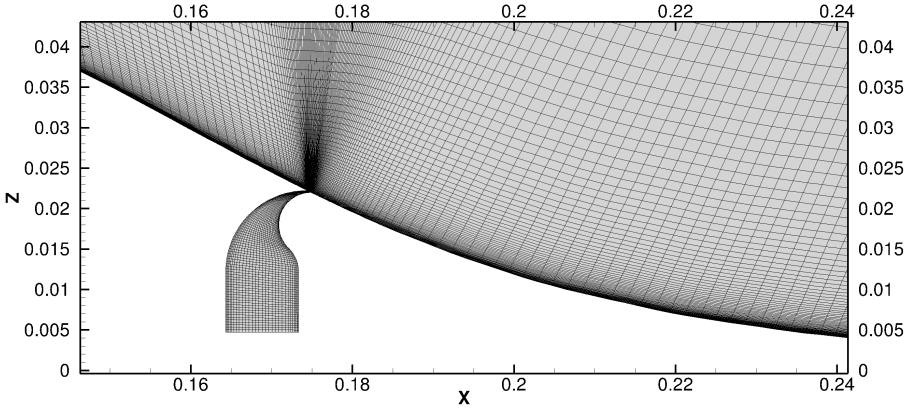

Figure 8: Injection mesh.

The objective of the optimisation is to reduce the pressure loses at the outlet of the domain through the mitigation of the recirculated flow region through flow injection. The location of the injection and inlet total pressure to the cavity are the main control parameters for the algorithm. The results of the surrogate model are shown in figure 9. The identified optimal configuration resides on actuation at $x_b = 0.138$ with a blow rate $R_b = 5\%$. The flow field correspondent to such structure are shown in figure 10.

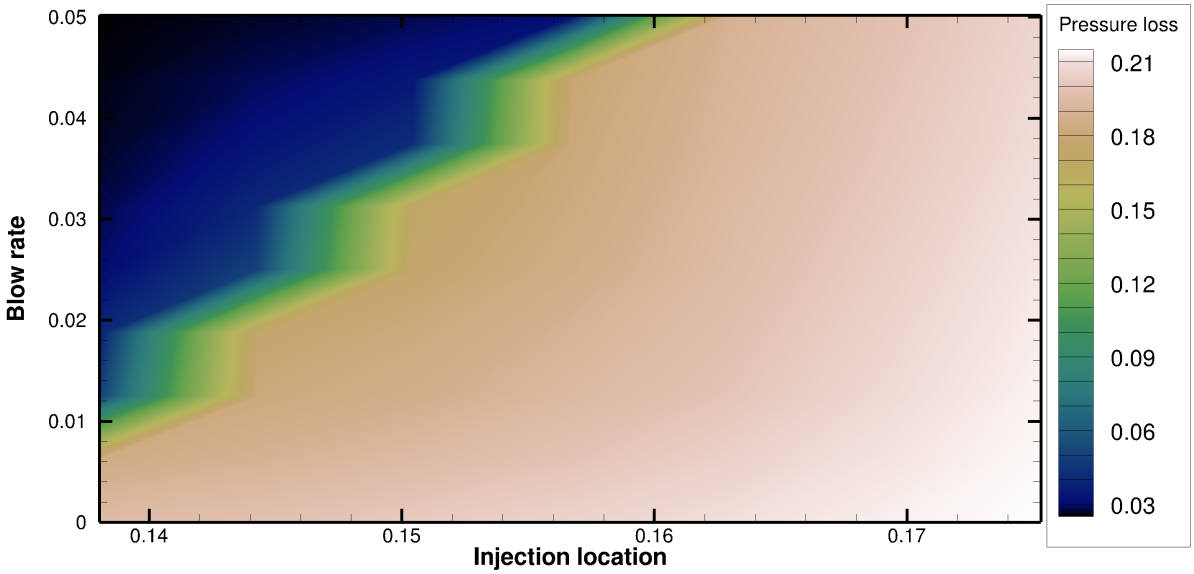

Figure 9: Surrogate model.

The optimization results further support the stability analysis performed where the optimum point of actuation sits in the furthest upstream boundary of our design space, slightly downstream of the hump summit and right before the boundary layer detachment. As identified through the most unstable mode description, the actuation at this location

DOI: 10.13009/EUCASS2019-492

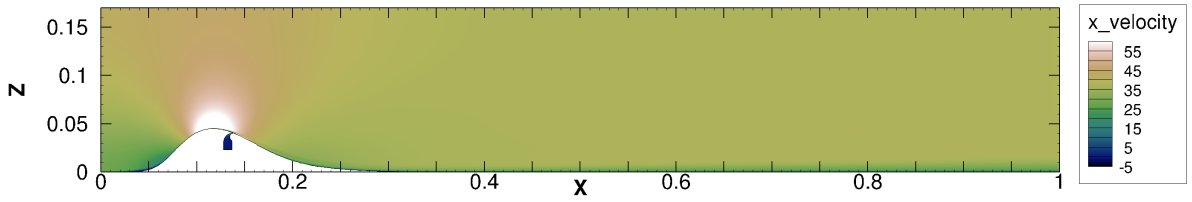

(a) u_x.

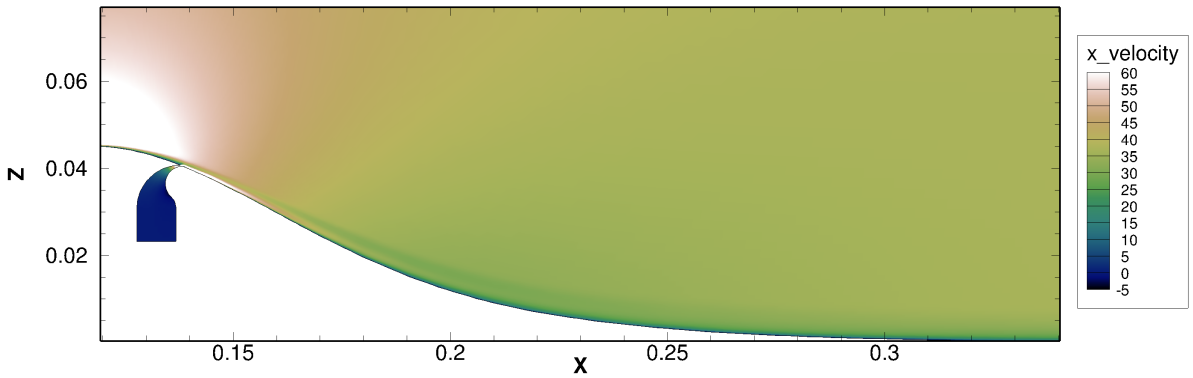

(b) u_x zoomed in.

Figure 10: u_x, optimal design.

heavily influences the boundary layer detachment process and once the injection pressure ratio provides enough momentum boost, the flow is able to remain attached and the viscous loses are mitigated. Considering the manufacturing complexity the identified optimum injection location also results in the most complicated design where the thickness between the hump summit and injection slot will be minimum. However, taking advantage of the surrogate model, figure 10, we can also identify further downstream location that could have still a deep impact on the pressure loses reduction.

Another interesting fact to notice on the surrogate model results, as shown in figure 9, is the strong transition in the dynamic pressure loss in some area where the location of the injection and the blow rate change by a small amount. Which highlights the strong sensitivity of the injection location and pressure on their ability to modulate the modes driving the separation. For illustration purposes, the results for various cases with small variations on the injection location and pressure ratio are shown in figures 11 and 12. These figures show the influence of small changes in both blow rate and location of the injection to the dynamic pressure loss. We can see that, when the dynamic pressure loss is low, the detachment is mainly controlled or influenced by the injection location. Additionally, based on these results, we can assume that there exist critical values for both the injection location, x_b, and blow rate, R_b, that strongly modulate the detachment and reattachment process and can have a strong impact reducing the dynamic pressure loss.

5. Conclusions

In this manuscript we analysed the boundary layer detachment phenomena in an expansion diffusion process as the one present in the aft portion of the suction side in a low pressure turbine. We used an ad-hoc wall mounted hump to characterize the boundary layer detachment and reattachment process at a wide variety of Reynolds numbers, 13980-448759.

We identified the eigenmodes associated to the boundary layer detachment through BiGlobal stability analysis together with the modes that had deeper influence on the growth and distribution of the recirculated flow region. The velocity contours and sensitivity maps identified that any modification introduced downstream of the hump summit could be able to alter the development of the mode driving the separation and deeply impact the recirculated flow region growth.

To characterize the impact of flow injection on the boundary layer detachment we introduced a cavity in the downstream surface of the hump that could discharge flow into the near wall region. Through a genetic algorithm optimization that also exploited a surrogate model we were able to confirm the results of the sensitivity analysis and

DOI: 10.13009/EUCASS2019-492

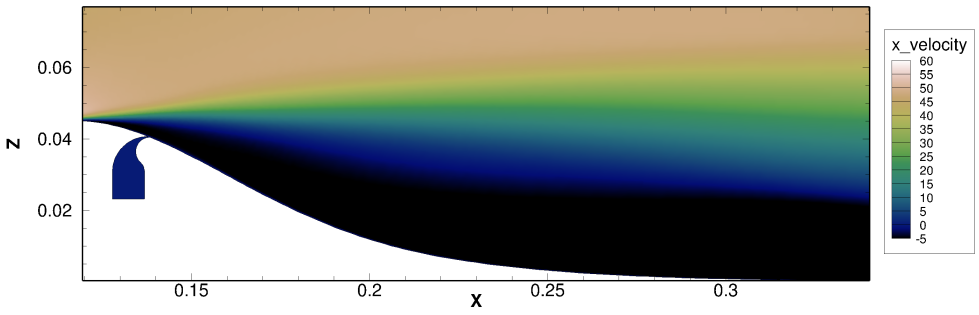

(a) $x_b = 0.138$, $R_b = 0.0\%$, $Pl = 0.197211$.

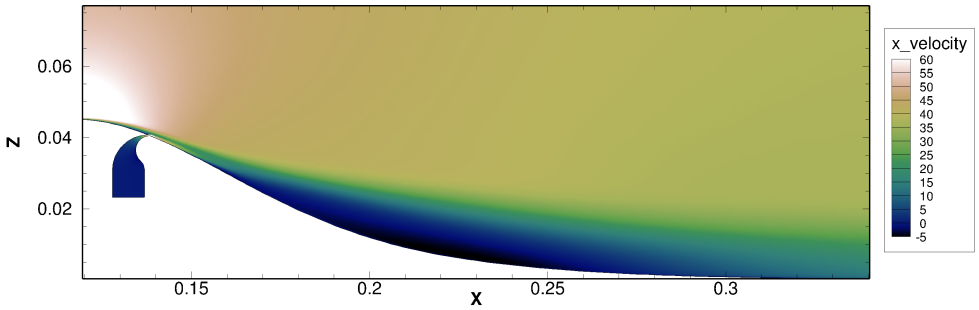

(b) $x_b = 0.138$, $R_b = 1.25\%$, $Pl = 0.049559$.

Figure 11: Influence of the blow rate R_b to the pressure loss near the jump.

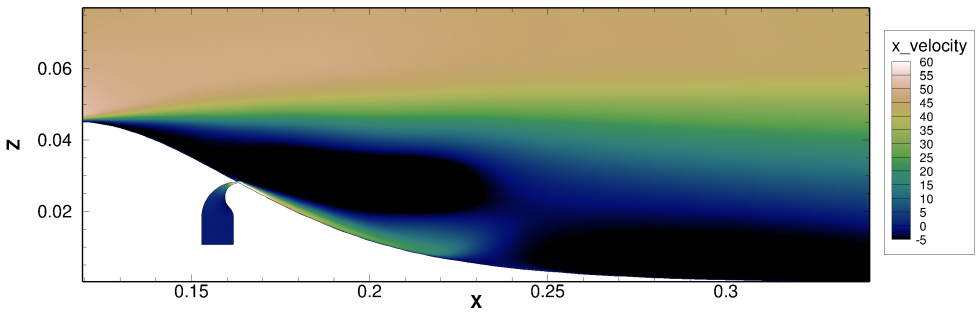

(a) $x_b = 0.157$, $R_b = 5.00\%$, $Pl = 0.188764$.

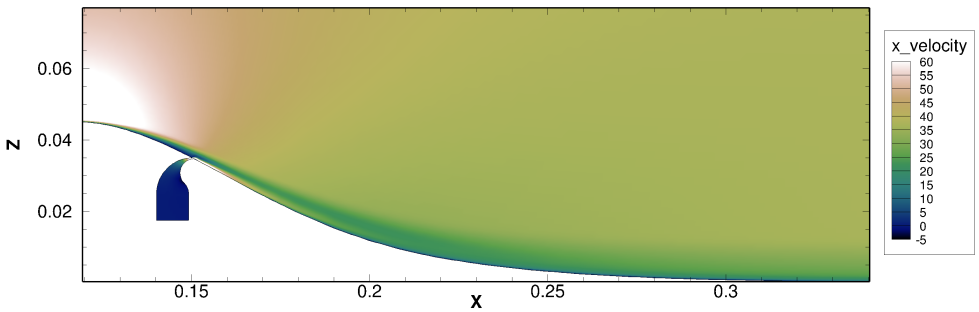

(b) $x_b = 0.150$, $R_b = 5.00\%$, $Pl = 0.0273964$.

Figure 12: u_x, optimal design.

DOI: 10.13009/EUCASS2019-492

the optimum location of injection was identified right at the origin of the most unstable mode. When introducing flow injection at sufficient pressure rate at that axial location the boundary layer detachment process could be completely mitigated and the pressure loss was minimal. In addition, the results of the surrogate model characterise the envelope of injection performance at various location describing not only the optimum but also suitable configurations for drag reduction with similar impact and easier practical implementation.

6. Acknowledgements

The authors acknowledge the financial support of SSeMID: *Stability and Sensitivity Methods for Industrial Design* funded by European Union's Horizon 2020 research and innovation program under the Marie Skłodowska-Curie grant agreement No. 675008.

References

[1] D. Barkley, H. M. Blackburn, and S. J. Sherwin. Direct optimal growth analysis for timesteppers. *International Journal for Numerical Methods in Fluids*, 57(9):1435–1458, 2008.

[2] J. P. Bons, R. Sondergaard, and R. B. Rivir. The Fluid Dynamics of LPT Blade Separation Control Using Pulsed Jets. 124(January 2002):77–85, 2016.

[3] O. Browne, G. Rubio, E. Ferrer, and E. Valero. Sensitivity analysis to unsteady perturbations of complex flows: A discrete approach. *International Journal for Numerical Methods in Fluids*, 76(12):1088–1110, 2014.

[4] J. Chomaz. Global Instabilities in Spatially Developing Flows: Non-Normality and Nonliearity. *Annual Review of Fluid Mechanics*, 37(1):357–392, 2005.

[5] E. Ferrer, O. M. F. Browne, and E. Valero. Sensitivity analysis to control the far-wake unsteadiness behind turbines. *Energies*, 10, 2017.

[6] E. Ferrer, J. de Vicente, and E. Valero. Low cost 3D global instability analysis and flow sensitivity based on dynamic mode decomposition and high-order numerical tools. *International Journal for Numerical Methods in Fluids*, 76(3):169–184, sep 2014.

[7] T. L. B. Flinois and T. Colonius. Optimal control of circular cylinder wakes using long control horizons. *Physics of Fluids*, 2015.

[8] F. Gianetti and P. Luchini. Structural sensitivity of the first instability of the cylinder wake. *Journal of Fluid Mechanics*, 581:167–197, 2007.

[9] C. Goldberg, D. Nalianda, D. MacManus, and P. Pilidis. Installed Performance Assessment of a Boundary Layer Ingesting Distributed Propulsion System at Design Point. pages 1–22, 2016.

[10] L. M. Gonzalez, E. Ferrer, and H.R. Diaz-Ojeda. Onset of three-dimensional flow instabilities in lid-driven circular cavities. *Physics of Fluids*, 29(6):064102, 2017.

[11] D. Greenblatt and I. J. Wygnanski. Control of flow separation by periodic excitation, 2000.

[12] D. C. Hill. A theoretical approach for analyzing the restabilization of wakes. In *AIAA Aersoapce Science Meeting Exhib. 30th, Reno, NV, AIAA Pap.*, volume 0067, 1992.

[13] L. Hultgren and D. Ashpis. Demonstration of Separation Delay with Glow Discharge Plasma Actuators. 2013.

[14] L. Huyse, S. L. Padula, R. M. Lewis, and W. Li. Probabilistic approach to free-form airfoil shape optimization under uncertainty. *AIAA Journal*, 40(9):1764–1772, 2002.

[15] M. C. Iorio, L. M. González, and E. Ferrer. Direct and adjoint global stability analysis of turbulent transonic flows over a NACA0012 profile. *International Journal for Numerical Methods in Fluids*, 76(3):147–168, 2014.

[16] J. Lake, P. King, and R. Rivir. Reduction of Separation Losses on a Turbine Blade with Low Reynolds Numbers. *37th Aerospace Sciences Meeting and Exhibit*, page 242, 1999.

[17] P. Luchini and A. Bottaro. Adjoint Equations in Stability Analysis. *Annual Review of Fluid Mechanics*, 46(1):493–517, 2014.

DOI: 10.13009/EUCASS2019-492

[18] T. J. Mackman and C. B. Allen. Comparison of Parameter Tuning Strategies for RBF Surrogate Models with Adaptive Sampling. *Evaluation*, (June):1–14, 2011.

[19] O. Marquet and L. Lesshafft. Identification of contributing flow regions for linear and nonlinear flow instabilities. *arXiv preprint*, 2015.

[20] O. Marquet, D. Sipp, and L. Jacquin. Sensitivity analysis and passive control of cylinder flow. *Journal of Fluid Mechanics*, 615:221–252, 2008.

[21] C. Mettot, F. Renac, and D. Sipp. Computation of eigenvalue sensitivity to base flow modifications in a discrete framework: Application to open-loop control. *Journal of Computational Physics*, 269:234 – 258, 2014.

[22] Ivan Padilla, Jorge Saavedra, Guillermo Paniagua, and Fabio Pinna. Analysis of the Boundary Layer Stability to Assess Flow Separation Control Capability in Low-Pressure Turbines. *6th European Conference on Computational Fluid Dynamics*, 2018.

[23] J. Périaux. Optimization Methods and Tools for Multi Objectives DESIGN using Evolutionary Algorithms and Game strategies. pages 1–44, 2014.

[24] J. Poggie. DC Glow Discharges: A Computational Study for Flow Control Applications. 2012.

[25] J. O. Pralits, L. Brandt, and F. Giannetti. Instability and sensitivity of the flow around a rotating circular cylinder. *Journal of Fluid Mechanics*, 2010.

[26] J. O. Pralits and A. Hanifi. Optimization of steady suction for disturbance control on infinite swept wings. *Physics of Fluids*, 2003.

[27] J. Saavedra and G. Paniagua. Transient Performance of Separated Flows: Characterization and Active Flow Control. *Journal of Engineering for Gas Turbines and Power*, 2019.

[28] P. J. Schmid and D. S. Henningson. *Stability and Transition in Shear Flows*. Springer, 2001.

[29] D. Sipp, O. Marquet, P. Meliga, and A. Barbagallo. Dynamics and control of global instabilities in open flows: a linearized approach. *Applied Mechanical reviews*, 63(3):1–26, 2010.

[30] R. J. Volino. Passive Flow Control on Low-Pressure Turbine Airfoils. *Journal of Turbomachinery*, 2003.

[31] D. Xiao and G. Papadakis. Nonlinear optimal control of bypass transition in a boundary layer flow. *Physics of Fluids*, 2017.